SST-induced surface wind variations over the Brazil/Malvinas Confluence: Satellite and in-situ observations

Hiroki Tokinaga[*], **Youichi Tanimoto**

Graduate School of Environmental Earth Science, Hokkaido University,

Sapporo, Japan

Shang-Ping Xie

International Pacific Research Center and Department of Meteorology,

University of Hawaii, Honolulu, Hawaii, USA

Journal of Climate

September 7, 2004, submitted

January 16, 2005, revised

March 22, 2005, accepted

---

[*]Current affiliation: Institute of Observational Research for Global Change, Japan Agency for Marine-Earth Science and Technology, Yokosuka, Japan

Corresponding author address: Hiroki Tokinaga, Institute of Observational Research for Global Change, Japan Agency for Marine-Earth Science and Technology, 2-15, Natsushima-cho, Yokosuka 237-0061, Japan
E-mail: tokinaga@jamstec.go.jp

Abstract

The confluence of the Brazil/Malvinas Currents maintains strong sea surface temperature (SST) fronts in the mid-latitude southwestern Atlantic year around. SST effects on near-surface stability and surface wind variations are examined in this region using satellite and in-situ datasets. Satellite observations show strong (weak) surface wind speeds over the warm Brazil (cold Malvinas) Current. A novel feature of this study is the construction of a high-resolution surface meteorological dataset based on historical ship observations. Analysis of this new in-situ dataset reveals increased (reduced) sea-air temperature difference over the Brazil (Malvinas) Current, indicating destabilization (stabilization) in the atmospheric boundary layer. These results are consistent with the SST-induced vertical mixing mechanism for wind adjustment. The SST effect on the near-surface atmosphere is observed both in the climatology and on interannual timescales in the Brazil/Malvinas Confluence. Along a zonal SST front at 49^{o}S northeast of the Malvinas/Falkland Islands, there is a collocated line of surface wind divergence, with moderate convergence to the north. Vertical mixing does not explain this divergence pattern since the prevailing surface winds are westerly blowing in parallel with the front. An additional mechanism is proposed for boundary-layer wind adjustment.

1. Introduction

Over extratropical oceans, basin-scale sea surface temperature anomalies (SSTAs) tend to display negative correlations with surface wind speed. Large-scale acceleration of surface westerlies in the wintertime extratropics often leads to an anomalous evaporative cooling of the ocean mixed layer (e.g., Wallace et al. 1990; Cayan 1992), a process that to first order, is attributable to chaotic atmospheric forcing of the surface ocean. In the central North Pacific, a horseshoe-like pattern of negative (positive) SST anomalies (Tanimoto et al. 1997; Mantua et al. 1997) is associated with enhanced (reduced) westerlies spatially organized in intrinsic atmospheric modes of variability such as the Pacific North American (PNA) pattern (Wallace and Gutzlar 1981). A similar relationship is found between the North Atlantic Oscillation (NAO) and tri-pole SSTA pattern in the North Atlantic (Wallace et al. 1990; Cayan 1992).

Near SST fronts of a width less than 1000 km, by contrast, a different pattern of air-sea interaction emerges characterized by positive correlations between anomalies of SST and surface wind speed (Xie 2004). For example, the prevailing southeasterly winds strengthen (weaken) over the warmer (colder) flank of the sharp SST front in the eastern equatorial Pacific (Wallace et al. 1989), a relationship most visible in tropical instability waves (TIWs) that cause the front to meander (Hayes et al. 1989; Xie et al. 1998; Liu et al. 2000; Chelton et al. 2001; Hashizume et al. 2001). Wallace et al. (1989) propose a vertical mixing mechanism for such an in-phase relationship between SST and surface wind: warm SST destabilizes the atmospheric planetary boundary layer (PBL) and mixes air with fast momentum from aloft to the surface, causing surface wind acceleration. On the other hand, cold SST stabilizes the PBL and weakens the vertical mixing, resulting in deceleration in surface wind. Direct atmospheric soundings render some support for this vertical mixing mechanism (Hashizume et al. 2002), but recent modeling results suggest an alternative mechanism: sea level pressure (SLP) anomalies developed downwind drive anomalous

winds in phase with SSTAs (Small et al. 2003), a mechanism consistent with limited buoy observations (Cronin et al. 2003).

Sweet et al. (1981) suggested the importance of vertical mixing in atmospheric wind adjustment based on aircraft observations across the SST front of the Gulf Stream. Their data show calm (strong) surface winds over the colder (warmer) flank of the SST front as a result of the stabilizing (destabilizing) of the atmospheric PBL. Similar ocean-atmospheric covariability has been detected over the other extratropical oceans in recent satellite observations. Xie et al. (2002) detect a winter air-sea pattern triggered by bathymetry on the continental shelf of the Yellow and East China Sea. Their analysis shows that bathymetric-induced warm (cold) SST is associated with strong (weak) surface winds and an increase (decrease) in local cloudiness. In their study of the meanders of the Kuroshio and its extension, Nonaka and Xie (2003) report increased (decreased) wind speed over anomalously warm (cold) SSTs. In their analysis of mesoscale variability over the Southern Ocean, O'Neill et al. (2003) obtain a SST-wind relationship in support of the vertical-mixing mechanism.

While rapid changes in wind and thermal structures of the PBL have been observed by limited atmospheric soundings across SST fronts of the Gulf Stream (Sweet et al. 1981) and the Agulhas Current (Jury and Walker 1988; Jury 1994), it is new satellite observations that allow a global survey for the first time revealing a robust and ubiquitous pattern of air-sea interaction around ocean fronts (Xie 2004; Chelton et al. 2004) that is unambiguously indicative of ocean influence on the atmosphere—in fact its characteristic positive correlation between SST and wind acts to dampen rather than create SST anomalies. From historical surface meteorological observations, Tanimoto et al. (2003) detect this damping effect of surface turbulent heat flux on SST over the Kuroshio-Oyashio extension, suggesting an oceanic origin for SST variations in this region where current advection is very important (Qiu 2000; Tomita et al. 2002), as opposed to the dominance of

atmospheric forcing via surface heat flux over the central North Pacific south of the Aleutian low.

While the remarkably consistent in-phase relationship between mesoscale SST and wind speed variability revealed from a recent global analysis of satellite data (Small et al. 2005) supports the vertical-mixing mechanism, space-borne remote sensing does not measure variables such as atmospheric stability, which is key to vertical mixing. Near-surface atmospheric stability is often measured by the SST-surface air temperature (SAT) difference, both variables routinely recorded in surface meteorological observations. Over most of the open ocean, shipboard observations are too sparse to resolve adequately ocean fronts, but in several regions ship activity is high enough to allow the construction of high-resolution datasets based on historical surface measurements. In those regions, surface meteorological variables including the stability parameter (SST-SAT) can be mapped in detail to study their adjustment to narrow ocean fronts and test the vertical-mixing mechanism.

The present study demonstrates this methodology of combined analysis of high-resolution satellite and surface observations with an example over the Brazil/Malvinas Confluence in the southwestern Atlantic. We choose to study this region because there are well-defined sharp fronts in the SST field and ship observations are abundant enough to map out surface meteorological variables in high resolution in the region. While O'Neill et al. (2003) study statistical SST-wind relation over the entire Southern Ocean from satellite, we aim at attaining a detailed regional analysis that complements space-borne remote sensing with surface measurements.

Briefly we discuss the regional oceanography using a new dataset for mean surface geostrophic current velocity based on drifter and satellite altimeter observations (Niiler et al. 2003). The Brazil Current is a western boundary current of the South Atlantic subtropical gyre, flowing south along the continental margin of South America and

advecting warm-saline water from the subtropics (Fig. 1). Against this warm current, the Malvinas Current, an offshoot of the Antarctic Circumpolar Current (ACC), transports cold-fresh water from the polar region along the east edge of the South American continental shelf. The confluence of the Brazil and Malvinas Currents generates remarkable SST fronts that are oriented meridionally west of 52°W and then zonally to the east (Legeckis and Gordon 1982; Garzoli 1993). In addition, a strong eastward jet associated with ACC forms a zonal SST front along 49°S northeast of the Malvinas/Falkland Islands. Although these currents and fronts have been studied rather extensively, to our knowledge, their influence on the atmosphere has not been discussed in the literature. South of 40°S, westerly winds prevail, blowing across and along the confluence fronts west and east of 52°W, respectively. Wind orientation relative to SST fronts is an important parameter for wind adjustment, because wind divergence (curl) is formed over the downwind (crosswind) SST gradient if the vertical mixing mechanism dominates (Chelton et al. 2001; O'Neill et al. 2003). Therefore, the wide range of wind orientation in the region makes it particularly interesting to study SST-wind interaction.

The rest of this paper is organized as follows. Section 2 introduces the satellite and in-situ datasets. Sections 3 and 4 investigate SST influence on surface wind and atmospheric stability in the climatological mean and interannual variability, respectively. Section 5 is a summary.

2. Data

a. Satellite measurements

We use the QuikSCAT vector wind product of Remote Sensing Systems (RSS) from July 1999 to June 2004, available daily on a 0.25° grid. For the period from January 1992 to December 1999 prior to QuikSCAT, we use the monthly F11 Special Sensor Microwave/Imager (SSM/I) product of RSS for scalar wind speed, available on a 0.25° grid

(Wentz 1997).

The Advanced Very High Resolution Radiometer (AVHRR) Pathfinder SST product (Vazquez et al., 1998) is obtained from the National Aeronautics and Space Administration/Jet Propulsion Laboratory Physical Oceanography Distributed Active Archive Center (NASA/JPL PO.DAAC), at monthly and 0.5^o resolution for January 1992 to December 1999. This period coincides with the F11-SSM/I wind measurements, permitting a study of interannual variability.

Finally, we use a sea surface height (SSH) product merging TOPEX/Poseidon (T/P) and European Remote Sensing (ERS) satellite altimeter observations, distributed by Archiving, Validation and Interpretation of Satellite Oceanographic data (AVISO) (Ducet et al. 2000). It is available from January 1993 to December 1999 on a 0.3^o grid and at 5-day intervals.

b. In-situ observations (HiRAC)

The Comprehensive Ocean-Atmosphere Data Set (COADS) (Woodruff et al. 1987) contains individual ship reports of surface meteorological measurements. Existing gridded COADS products apply the same gridding procedures over the globe and do not have the necessary resolution to represent narrow ocean fronts. Because of its proximity to South America, COADS ship reports are dense enough for a high-resolution climatology over the Brazil-Malvinas Confluence region. Following the gridding procedure of Iwasaka and Hanawa (1990) and Tanimoto et al. (1997), we construct a monthly dataset on a 0.5^o grid for a 38-year period of January 1960 to December 1997, a significant improvement over existing gridded COADS products with resolutions of 2^o or coarser. At a given grid point, we use only the ship reports that depart from the monthly climatological mean by less than 3 standard deviations in the 1^o x 1^o box. The final monthly climatology is obtained by averaging data for the 38-year period.

Figure 2 compares in scatter plot the mean SST and wind speed derived from satellite observations and our new High-resolution, Regionally Analyzed COADS (HiRAC) for the southwestern Atlantic ($40^oW–70^oW$, $30^oS–58^oS$). Annual mean climatologies on 0.5^o grid are used in Fig. 2. For SST, the correlation coefficient between the AVHRR and HiRAC products is 0.997, significant at the 99% level. The systematic bias between HiRAC and AVHRR is negligibly small ($+0.01^oC$), and the root-mean-squared (rms) difference is 0.47^oC. For wind speed, the correlation coefficient is 0.86 between SSM/I and HiRAC. The bias between HiRAC and SSM/I is -0.23 m s^{-1}, and the rms difference is 0.57 m s^{-1}, much smaller than the spatial variations to be discussed in the present study. Besides those variables that satellites now routinely measure, most importantly, the HiRAC includes SAT and SLP, variables important for studying atmospheric adjustment to SST variations. In addition, surface latent and sensible heat fluxes (Qe, Qh) are calculated from individual ship reports by aerodynamic bulk formula (Kondo 1975).

3. Climatology

a. SST and wind

Figure 3 shows annual-mean climatology of AVHRR SST and QuikSCAT surface wind velocity over the southwestern Atlantic. The westerly wind prevails south of 40^oS, whose curls drive ocean gyre circulations. Scalar wind speed is visibly modulated by ocean fronts (Fig. 3a). In particular, wind speed minimum is roughly collocated with the cold tongue of the Malvinas Current, with increased wind speed on both flanks. The zonal difference in scalar wind speed between the Brazil and Malvinas Currents corresponds to 2 – 2.5 m s^{-1}, which is consistent with that observed across the Kuroshio front (Xie et al. 2002; Nonaka and Xie 2003). Further offshore, wind speed reaches a meridional maximum on the warmer and a minimum on the colder flank of the zonal SST front centered at 49^oS. Cross-frontal variations in wind speed are unclear along the SST front to the north, by

contrast, presumably partially masked by the rapid southward increase in background wind speed. As will be shown shortly, atmospheric stability displays large cross-frontal changes in HiRAC observations.

QuikSCAT observes surface wind stress that arises from the relative air motion to ocean current (Kelly et al. 2001; Chelton et al. 2004). For the following reasons, the SST-frontal modulation of QuikSCAT wind does not seem to be dominated in this region by the ocean current effect. First, ocean currents do not generally exceed 0.5 m s^{-1} in the climatological map of Figure 1, too small to account for the observed cross-frontal changes in wind, up to 2 m s^{-1} in magnitude. Second, both the Brazil and Malvinas Currents are roughly perpendicular to the prevailing westerlies that are much faster, rendering ocean currents not effective in modulating wind speed. Third, the maximum eastward current along 49^{o}S in 40^{o}W – 50^{o}W would produce an apparent minimum in QuikSCAT "wind" speed, but this current effect is both too small in magnitude and inconsistent in spatial distribution with the observed wind speed minimum that is located slightly to the south. Finally, there are strong divergence and convergence patterns over these currents. As discussed by Chelton et al (2004), this is a good indication that ocean currents are not affecting the stress since surface ocean currents are essentially nondivergent.

SST fronts also leave a clear signature in QuikSCAT wind divergence (Fig. 3b). The westerly winds blow roughly perpendicular across the cold tongue of the Malvinas Current, convergent on the windward side of the cold tongue and divergent on the leeward side. This pattern of convergence and divergence is associated with the wind deceleration over the cold tongue. O'Neill et al. (2003) detect a robust relationship between downwind gradient and wind divergence over the Southern Ocean and suggest that it supports the vertical mixing mechanism: a downwind increase in SST causes surface wind to accelerate, inducing wind divergence, and vice versa.

While the downwind SST gradient explains the wind divergence pattern along

meridionally oriented SST fronts, conspicuous wind divergence is found on the zonally oriented SST front along 49^{o}S in 40^{o}W – 50^{o}W year around, flanked by convergence on the sides (Figs. 3b and 4a). Meridional-wind divergence in the same region (Fig. 4b) accounts for nearly all the total divergence throughout the year (Fig. 4a) despite the fact that zonal winds are 3 times larger in speed than meridional ones on the 49^{o}S front (Figs. 4c and 4d). The surface meridional winds over this region are southerlies (northerlies) from April (October) to September (March) with increasing over the warmer (colder) flank of the 49^{o}S front (Fig. 4d). These wind directions depend on large-scale SLP gradient. If only the vertical-mixing mechanism is at work over the warm-to-cold SST front as shown by O'Neill et al. (2003), the northerlies should lead to convergence rather than divergence from October to the following March. However, surface wind divergence remains positive and strong on the SST front year around (Figs. 4a and 4b). Therefore, some other processes are involved in this divergence generation.

We propose the following mechanism for wind divergence when winds blow in parallel with the SST front. As an initial state, we assume that the background westerly winds are in geostrophic balance with broad-scale pressure gradients, and then add a zonal SST front (Fig. 5). Since the scale of atmospheric adjustment (~1000 km) is much greater than that of SST fronts (~100 km), air temperature will take a smoother distribution across the front than SST. This leaves the atmosphere unstably and stably stratified north and south of the front, respectively (Xie 2004)—a stability distribution confirmed by HiRAC observations along the 49^{o}S front (Fig. 6b). As a result, vertical mixing and westerlies intensify (weaken) on the warmer (colder) flank of the front. Acting upon these zonal wind perturbations induced by the SST front (small solid arrows in Fig. 5), the Coriolis force induces southerly (northerly) wind anomalies (open arrows in Fig. 5), thereby causing surface divergence along the SST front and convergence on either side. Supporting this hypothesis, Figure 4d shows a localized maximum in southerly wind velocity north of the

49°S front, which explains the zonal divergence along the front. Indeed, consistent with this hypothesis, the southerly wind speed reaches a local maximum over the southern half of the SST, inducing divergence and convergence to the south and north, respectively. For reasons unclear at this time, the sub-geostrophic adjustment south of the front is not obvious in the observed divergence field.

b. Static stability

The SST and wind speed distributions and their relationship based on historical ship observations (HiRAC) closely resemble those observed by satellite (Fig. 6a). For example, the wind speed minima along the cold Malvinas Current and south of the 49°S SST front are just two examples. This close similarity between the two independent sets of observations gives us confidence in both.

Most unique to HiRAC is the stability parameter (SST-SAT) that it offers (Fig. 6b). SST-frontal effect on this stability parameter is very clear, being positive—the atmosphere is unstably stratified—in the warm tongue of the Brazil Current and negative in the cold tongue of the Malvinas Current near the South American coast. Figure 7 shows the meridional cross-frontal structure of HiRAC SST, SAT, SST-SAT, wind speed, and net turbulent heat flux (Qe+Qh) averaged in 35°W – 47°W. Consistent with Xie's (2004) hypothesis for atmospheric adjustment to a narrow SST front, the atmospheric stratification changes from stable to unstable as one moves from the cold to warm flank of the 49°S front. The cross-frontal changes in (SST-SAT) and net surface heat flux (Qe+Qh) are typically about 1°C and 80 W m^{-2}, respectively (Fig. 7b). A similar change in stability is observed across the 42°S front while its effect on annual-mean scalar wind speed is unclear. This is because the gradient of southward-increasing background wind speed presumably masks the SST-frontal effect. The cross-front transition of atmospheric stability revealed by HiRAC is consistent with the vertical-mixing hypothesis, in which stability modulates the

vertical profile of wind and surface wind velocity. Indeed, both QuikSCAT and HiRAC observations generally show increased (decreased) wind speed over regions of negative (positive) stability parameter. While meridional spatial change in those variables is depicted here, the stability-wind correlation on interannual time scales will be discussed for the meridional SST front along 53.25 ^{o}W in Section 4.

Figure 8 offers a close look into the ocean-atmospheric structure along 42^{o}S near the confluence point of the Brazil-Malvinas Currents. SAT is indeed smoother than the SST profile with reduced zonal variations, resulting in stable stratification within the cold tongue and unstable one on its eastern edge. Wind speed increases by 2 m s^{-1} over the same zonal distance. A product of wind speed and sea-air differences, Qe+Qh varies even more, from 10 W m^{-2} at the center of the cold tongue to near 140 W m^{-2} on its eastern edge.

Figure 9 shows the annual cycle in the HiRAC SST, SST-SAT, and wind speed along 42^{o}S. At this latitude, the Brazil and Malvinas Currents are centered at 52^{o}W and 56^{o}W, respectively, with an SST front in between (Fig. 9a). While the SST's annual range reaches more than -6 ^{o}C, the SST difference across this front remains near constant at about 5 ^{o}C throughout the year. On the warmer (colder) flank of the SST front, the SST-SAT difference is positive (negative) throughout the year (Fig. 9b). While atmospheric stability and wind speed remain remarkably constant over the cold Malvinas Current (at –0.5^{o}C and 7 m s^{-1}, respectively), large seasonal variations are observed over the warm Brazil Current. During the local cold seasons from March to October, the SST-SAT difference exceeds +2 ^{o}C over the Brazil Current, with a well-defined maximum on the eastern edge of the SST front. Associated with this eastward increase in SST-SAT, wind speed accelerates rapidly from 7 m s^{-1} to more than 10 m s^{-1} across the front (Fig. 9c).

c. Sea level pressure

Lindzen and Nigam (1987) propose that in the tropics, SST variations affect surface

winds through their effects on air temperature and SLP in the PBL (Small et al. 2003). Figure 10 displays SLP based on our HiRAC. While there is a weak indication of a SLP maximum over the Malvinas Current cold tongue, the SLP contours are generally zonally oriented to be in geostrophic balance with the prevailing westerly winds. Because of strong meridional gradients in the background and noises due to insufficient sampling, we are unable to determine from this HiRAC SLP distribution whether the local SST effect on SLP is an important mechanism for frontal-scale wind variations over the region.

4. Interannual variability

Air-sea co-variations in space described above indicate a considerable influence of SST fronts on surface stability and wind. This section extends the analysis to temporal correlation to corroborate this finding. In the extratropics on the basin scale, the atmospheric forcing is the dominant mechanism for SST variability, resulting in negative correlation between SST and surface wind speed. Near SST fronts, by contrast, stability-induced vertical mixing becomes important leading to positive correlation between SST and wind speed (Xie 2004). Therefore, we need to remove the basin-scale atmospheric forcing from interannual variations in order to study surface wind response to shifts in SST fronts. We use surface wind speed anomaly averaged in 35^{o}S – 50^{o}S, 40^{o}W – 70^{o}W, a region of largest variance of surface wind speed (not shown), to represent large-scale atmospheric forcing. Then variability linearly correlated with this reference time series is removed from monthly anomalies of ocean and atmospheric variables of interest. Finally, a 7-month running mean is applied to the residual anomalies. The resultant "short-scale" variability retains roughly half of standard deviations of the unfiltered anomalies over much of the region (Fig. 11). SST variance is high along the mean SST fronts for both unfiltered and filtered anomalies, with typical standard deviation of 1.0^{o}C and 0.5^{o}C, respectively. This collocation of high SST variance and SST fronts

indicates an important role played by ocean currents. In fact, the confluence point of the Brazil and Malvinas Currents, where they separate from the western boundary, displays large interannual variations (Legeckis and Gordon 1982; Olson et al. 1988), which are apparently responsible for the maximum SST variance there (Fig. 11).

Figure 12 shows time-latitude sections of filtered anomalies of SST, surface wind speed, and SSH along the meridional SST front (53.25^{o}W) on the eastern flank of the Malvinas Current cold tongue. SST and wind speed are visibly correlated, with correlation coefficients exceeding +0.72 north of 41^{o}S (Fig. 13). The maximum correlation of +0.83 is reached at 38^{o}S, the point of the largest SST variance. This in-phase relationship between SST and wind speed again supports the vertical mixing mechanism. SSH is apparently correlated with both SST and wind speed. In particular, all three fields show a southward (northward) propagating tendency south (north) of 44^{o}S. By analogy to previous studies (e.g., Nonaka and Xie 2003; Vecchi et al. 2004; Small et al. 2005), this co-variability presumably reflects ocean mesoscale variability causing SST and then surface wind to change.

Figure 14 shows the time series of a few key surface variables from in-situ HiRAC observations, averaged in the region of maximum SST variance (53.25^{o}W, 36^{o}S – 39^{o}S). Unlike Fig. 12, unfiltered monthly anomalies are used here (the spatial filter is not necessary because the high SST variance is mostly due to shifts in the sharp SST front). Air temperature is correlated with SST at +0.52, a correlation coefficient that exceeds the 95% significance level (Fig. 14a). Sea-air temperature difference (Fig. 14b) is even more highly correlated with SST at +0.67 while its correlation with air temperature is only -0.18. This suggests that SST controls the near-surface stability over the Brazil/Malvinas Confluence.

The correlation coefficient between wind speed and atmospheric stability is +0.37, which is above the 90 % significance level (Fig. 14b). This correlation coefficient becomes

+0.52 if data in 1995 are excluded. This correlation in time is consistent with the vertical mixing mechanism for surface wind modulation by SST fronts.

5. Summary

We have studied the influence of the Brazil/Malvinas Confluence on local winds by using high-resolution satellite observations and constructing a high-resolution, regionally analyzed surface-meteorological dataset based on historical ship reports. The Brazil and Malvinas Currents and their eastward extension maintain robust SST fronts year round in the region. Our HiRAC observations reveal a clear transition in sea-air temperature difference across all these fronts, with the surface atmosphere reducing its stability from the cold to warm flank. Wind speed generally increases on the unstable warm flank because of enhanced vertical mixing while decreasing on the stable cold flank of the fronts. This cross-frontal transition in stability is consistent with Xie's (2004) hypothesis that it results from the disparity in atmospheric and ocean frontal scales, providing supporting evidence for the vertical mixing mechanism of the cross-frontal adjustment of wind. Our results add to a growing literature showing an unambiguous ocean-to-atmospheric feedback that is characterized by positive correlation between SST and surface wind speed, a correlation opposite to what is observed in coarse-resolution datasets without sharp SST fronts (Xie 2004). This positive SST-wind correlation is observed in both spatial and interannual variability. A unique contribution of this study is its demonstration of the utility of high-resolution analysis of historical ship observations: while the SST front's influence on local winds has been well documented, the in-situ observations allow a mapping of the climatological cross-frontal structure of atmospheric stability for the first time, a parameter key to determining the mechanism for satellite-observed wind variations.

The zonal SST front along 49^{o}S is roughly in parallel with the prevailing westerlies. Figure 1 suggests that the axis of the eastward current is collocated with this front, the

strong wind stress curl induced by the front (Fig. 15) will induce a Sverdrup circulation with a western boundary current that may help the Malvinas Current to overshoot. This possible feedback from the front-induced wind variations remains to be investigated. Besides the wind curl response, conspicuous wind divergence is observed on this zonal front and is flanked by convergence on either side. We have proposed a mechanism for this wind divergence that involves the Coriolis effect acting on the SST-induced acceleration/deceleration of wind.

SST gradients may affect extratropical storm tracks through the effect on PBL temperature and baroclinicity (e.g., Inatsu et al., 2002; Tanimoto et al., 2003). In a regional atmospheric model, for example, Xie et al. (2002) show that the Kuroshio front affects the growth and path of an extratropical cyclone. The mid-latitude western South Atlantic is a region of cyclogenesis (Sinclair 1994). Nakamura and Shimpo (2004) present observational evidence for a dominant role of SST fronts in shaping the South Hemisphere storm tracks, one that partially supported by recent general circulation model experiments of Inatsu and Hoskins (2004). The interaction of SST fronts and atmospheric storm tracks is a subject of our ongoing research.

Acknowledgements

We wish to thank Drs. M. Ikeda, N. Ebuchi, Y. Fujiyoshi, K. Takeuchi for their discussions and suggestions, Dr. N. Maximenko for supplying the ocean current dataset, and Dr. J. Hafner for data processing. We also thank Dr. D. Chelton and an anonymous reviewer for detailed comments. This work was supported by Grand-in-Aid for Scientific Research defrayed by the Ministry of Education, Culture, Sports, Science and Technology of Japan (15540416), Japan Agency for Marine-Earth Science and Technology, Japan Society for the Promotion of Science (JSPS) Visiting Fellow Program, and NASA. IPRC publication Number 318 and SOEST publication Number 6569.

References

Cayan, D. R., 1992: Latent and sensible heat flux anomalies over the northern oceans: Driving the sea surface temperature. *J. Phys. Oceanogr.*, **22**, 859-881.

Chelton, D.B., S. K. Esbensen, M. G. Schlax, N. Thum, M. H. Freilich, F. J. Wentz, C. L. Gentemann, M. J. McPhaden, and P. S. Schopf, 2001: Observations of coupling between surface wind stress and sea surface temperature in the eastern tropical Pacific. *J. Climate*, **14**, 1479-1498.

___, M. G. Schlax, M. H. Freilich, and R. F. Milliff, 2004: Satellite radar measurements reveal short-scale features in the wind stress field over the world ocean. *Science*, **303**, 978-983.

Cronin, M. F., S. -P. Xie, and H. Hashizume, 2003: Barometric pressure variations associated with eastern Pacific tropical instability waves. *J. Climate*, **16**, 3050-3057.

Ducet, N., P. Y. Le Traon, and G. Reverdin, 2000: Global high-resolution mapping of ocean circulation from the combination of T/P and ERS-1/2. *J. Geophys. Res.*, **105**, 19 477-19 498.

Garzoli, S. L., 1993: Geostrophic velocities and transport variability in the Brazil/Malvinas Confluence. *Deep-Sea Res.*, **40**, 1379-1403.

Hashizume, H., S. -P. Xie, W. T. Liu, and K. Takeuchi, 2001: Local and remote atmospheric response to tropical instability waves: A global view from the space. *J. Geophys. Res.*, **106**, 10 173-10 185.

___, ___, M. Fujiwara, M. Shiotani, T. Watanabe, Y. Tanimoto, W. T. Liu, and K. Takeuchi, 2002: Direct observations of atmospheric boundary layer response to SST variations associated with tropical instability waves over the eastern equatorial Pacific. *J. Climate*, **15**, 3379-3393.

Hayes, S. P., M. J. McPhaden, and J. M. Wallace, 1989: The influence of sea surface temperature on surface wind in the eastern equatorial Pacific. *J. Climate*, **2**, 1500-1506.

Inatsu, M., H. Mukougawa, and S. -P. Xie, 2002: Tropical and extratropical SST effects on the midlatitude storm track. *J. Meteor. Soc. Japan*, **80**, 1069-1076.

___, and B. J. Hoskins, 2004: The zonal asymmetry of the southern hemisphere winter storm-track. *J. Climate*, **17**, 4882–4892.

Iwasaka, N., and K. Hanawa, 1990: Climatologies of marine meteorological variables and surface fluxes in the North Pacific computed from COADS. *Tohoku Geophys. J.*, **33**, 185-239.

Jury, M., and N. Walker, 1988: Marine boundary layer modification across the edge of the Agulhas Current. *J. Geophys. Res.*, **93**, 647-654.

___, 1994: A thermal front within the marine atmospheric boundary layer over the Agulhas Current south of Africa: Composite aircraft observations. *J. Geophys. Res.*, **99**, 3297-3304.

Kelly, K. A., S. Dickinson, M. J. McPhaden, and G. C. Johnson, 2001: Ocean currents evident in satellite wind data. *Geophys. Res. Lett.*, **28**, 2469-2472.

Kondo, J., 1975: Air-sea bulk transfer coefficients in diabatic conditions. *Boundary-Layer Meteor.*, **9**, 91-112.

Legeckis, R., and A. L. Gordon, 1982: Satellite observations of the Brazil and Falkland Currents, 1975 to 1976 and 1978. *Deep-Sea Res.*, **29**, 375-401.

Lindzen, R. S., and S. Nigam, 1987: On the role of sea surface temperature gradients in forcing low-level winds and convergence in the tropics. *J. Atmos. Sci.*, **44**, 2418-2436.

Liu, W. T., X. Xie, P. S. Polito, S. -P. Xie, and H. Hashizume, 2000: Atmospheric manifestation of tropical instability waves observed by QuikSCAT and Tropical Rain Measuring Mission. *Geophys. Res. Lett.*, **27**, 2545-2548.

Mantua, N. J., S. R. Hare, Y. Zhang, J. M. Wallace, and R. C. Francis, 1997: A Pacific interdecadal climate oscillation with impacts on salmon production. *Bull. Amer. Meteor. Soc.*, **78**, 1069-1079.

Nakamura, H., and A. Shimpo, 2004: Seasonal variations in the Southern Hemisphere storm tracks and jet streams as revealed in a reanalysis dataset. *J. Climate*, **17**, 1828–1844.

Niiler, P. P., N. A. Maximenko, and J. C. McWilliams, 2003: Dynamically balanced absolute sea level of the global ocean derived from near-surface velocity observations. *Geophys. Res. Lett.*, **30**, 2164, doi:10.1029/2003GL018628.

Nonaka, M., and S. -P. Xie, 2003: Co-variations of sea surface temperature and wind over the Kuroshio and its extension: Evidence for ocean-to-atmospheric feedback. *J. Climate*, **16**, 1404-1413.

Olson, D. B., G. P. Podesta, R. H. Evans, and O. B. Brown, 1988: Temporal variations in the separation of Brazil and Malvinas Currents. *Deep-Sea Res.*, **35**, 1971-1990.

O'Neill, L. W., D. B. Chelton, and S. K. Esbensen, 2003: Observations of SST-induced perturbations of the wind stress field over the Southern Ocean on seasonal timescales. *J. Climate*, **16**, 2340-2354.

Qiu, B., 2000: Interannual variability of the Kuroshio Extension system and its impact on the wintertime SST field. *J. Phys. Oceanogr.*, **30**, 1486-1502.

Sinclair, S. R., 1994: An objective cyclone climatology for the southern hemisphere. *Mon. Wea. Rev.*, **122**, 2239-2256.

Small, R. J., S. -P. Xie, and Y. Wang, 2003: Numerical simulation of atmospheric response to Pacific tropical instability waves. *J. Climate,* **16**, 3722-3740.

___, S. -P. Xie, and J. Hafner, 2005: Satellite observations of mesoscale ocean features and co-propagating atmospheric surface fields in the tropical belt. *J. Geophys. Res.*, **110**, C02021, doi:10.1029/2004JC002598.

Sweet, W., R. Fett, J. Kerling, and P. La Violette, 1981: Air-Sea interaction effects in the lower troposphere across the north wall of the Gulf Stream. *Mon. Wea. Rev.*, **109**, 1042–1052.

Tanimoto, Y., N. Iwasaka, and K. Hanawa, 1997: Relationship between sea surface temperature, the atmospheric circulation and air-sea fluxes on multiple time scales. *J. Meteor. Soc. Japan*, **75**, 831-849.

___, H. Nakamura, T. Kagimoto, and S. Yamane, 2003: An active role of extratropical sea surface temperature anomalies in determining anomalous turbulent heat flux. *J. Geophys. Res.*, **108**, 3304, doi:10.1029/2002JC001750.

Tomita, T., S. -P. Xie, and M. Nonaka, 2002: Estimates of surface and subsurface forcing for decadal sea surface temperature variability in the mid-latitude North Pacific. *J. Meteor. Soc. Japan*, **79**, 1289-1300.

Vazquez, J., K. Perry, and K. Kilpatrick, 1998: NOAA/NASA AVHRR oceans Pathfinder sea surface temperature data set user's reference manual. Tech. Rep. D-14070, Jet Propulsion Laboratory, Pasadena, CA, 82 pp.

Vecchi, G. A., S. -P. Xie, and A. S. Fischer, 2004: Ocean-atmosphere covariability in the western Arabian Sea. *J. Climate*, **17**, 1213–1224.

Wallace, J. M., and D. S. Gutzler, 1981: Teleconnections in the geopotential height field during the Northern Hemisphere winter. *Mon. Wea. Rev.*, **109**, 784-812.

___, T. P. Mitchell, and C. Deser, 1989: The influence of sea surface temperature on surface wind in the eastern equatorial Pacific: Seasonal and interannual variability. *J. Climate*, **2**, 1492-1499.

___, C. Smith, and Q. Jiang, 1990: Spatial patterns of atmosphere-ocean interaction in the northern winter. *J. Climate*, **3**, 990-998.

Wentz, F. J., 1997: A well-calibrated ocean algorithm for SSM/I. *J. Geophys. Res.*, **102**, 8703-8718.

Woodruff, S. D., R. J. Slutz, R. L. Jenne, and P. M. Steurer, 1987: A comprehensive ocean-atmosphere dataset. *Bull. Amer. Meteor. Soc.*, **68**, 521-527.

Xie, S. -P., 2004: Satellite observations of cool ocean-atmosphere interaction. *Bull. Amer.*

Meteor. Soc., **85**, 195-208.

___, M. Ishiwatari, H. Hashizume, and K. Takeuchi, 1998: Coupled ocean-atmospheric waves on the equatorial front. *Geophys. Res. Lett.*, **25**, 3863-3866.

___, J. Hafner, Y. Tanimoto, W. T. Liu, H. Tokinaga, and H. Xu, 2002: Bathymetric effect on the winter climate of the Yellow and East China Seas. *Geophys. Res. Lett.*, **29**, 2228, doi: 10.1029/2002GL015884.

Figure captions

Fig. 1. Mean geostrophic ocean current velocity (arrows in cm s^{-1}) and speed (color in cm s^{-1}) based on drifter and satellite altimeter observations. Annual mean climatology of AVHRR SST is superimposed in contours at 1^{o}C intervals.

Fig. 2. Scatter plots for comparison of annual mean climatologies of SST and surface wind speed over the southwestern Atlantic (40^{o}W – 70^{o}W, 30^{o}S – 58^{o}S): (a) AVHRR and HiRAC SST, and (b) SSM/I and HiRAC wind speed.

Fig. 3. Annual mean climatologies of (a) scalar wind speed (color in m s^{-1}) and (b) surface wind divergence (color in 10^{-6} s^{-1}) observed by QuikSCAT, superimposed on mean SST (contours in ^{o}C) and surface wind velocity (arrows in m s^{-1}).

Fig. 4. Climatological annual cycle averaged in 40^{o}W – 50^{o}W. (a) Total surface-wind divergence (10^{-6} s^{-1}), (b) divergence due to the meridional velocity only (10^{-6} s^{-1}), (c) surface zonal and (d) meridional velocities (m s^{-1}). SST contours are superimposed at 1^{o}C intervals.

Fig. 5. Schematic for surface wind divergence generated by winds blowing in parallel to the SST front (shaded box). Block arrow on the left: background westerly wind; solid arrows: wind perturbations induced by the SST front; open arrows: meridional winds induced by the Coriolis force acting on the zonal wind perturbations.

Fig. 6. (a) Same as Fig. 3a but for HiRAC. (b) Sea-air temperature difference (SST-SAT; color in ^{o}C) calculated from HiRAC, superimposed on mean HiRAC SST.

Fig. 7. Cross-frontal structure. (a) SST (solid in ^{o}C) and surface air temperature (dashed in ^{o}C) averaged in 35^{o}W – 47^{o}W as a function of latitude. (b) SST-SAT (thick solid in ^{o}C), scalar wind speed (dashed in m s^{-1}), and surface latent and sensible heat fluxes (thin solid in W m^{-2}). All from HiRAC annual-mean climatology.

Fig. 8. Same as Fig. 7 but for HiRAC annual-mean climatologies along 42^{o}S as a function of longitude.

Fig. 9. Annual cycle along 42°S of (a) SST (contour intervals of 1 °C), (b) SST-SAT (contour intervals of 0.5 °C; shading > 0 °C), and (c) surface wind speed (contour intervals of 0.5 m s^{-1}; shade > 6.5 m s^{-1}) as a function of longitude and calendar month. All from HiRAC climatology.

Fig. 10. Same as Fig. 6a but for HiRAC sea level pressure (solid contours and gray shade in hPa), superimposed on mean HiRAC SST (dashed contours at 2°C intervals).

Fig. 11. Standard deviations (color in °C) for (a) unfiltered and (b) filtered monthly AVHRR SST anomalies, superimposed on mean AVHRR SST white contours at 1 °C intervals.

Fig. 12. Latitude-time sections of filtered anomalies of (a) AVHRR SST (°C), (b) SSM/I scalar wind speed (m s^{-1}), and (c) satellite altimeter SSH (cm) along the meridional SST front at 53.25°W.

Fig. 13. Correlation coefficient between AVHRR SST and SSM/I surface wind anomalies along 53.25°W.

Fig. 14. Time series of anomalies of (a) SST (solid) and SAT (dashed), and (b) SST-SAT (solid) and scalar wind speed, averaged in a region of maximum SST variance (53.25°W, 36°S – 39°S). All from HiRAC and normalized with their respective standard deviations.

Fig. 15. Same as Fig. 3a but for annual mean climatologies of wind stress curl (color in N m^{-3}) computed from QuikSCAT wind, superimposed on mean SST (contours in °C) and mean geostrophic ocean current velocity (arrows in cm s^{-1}).

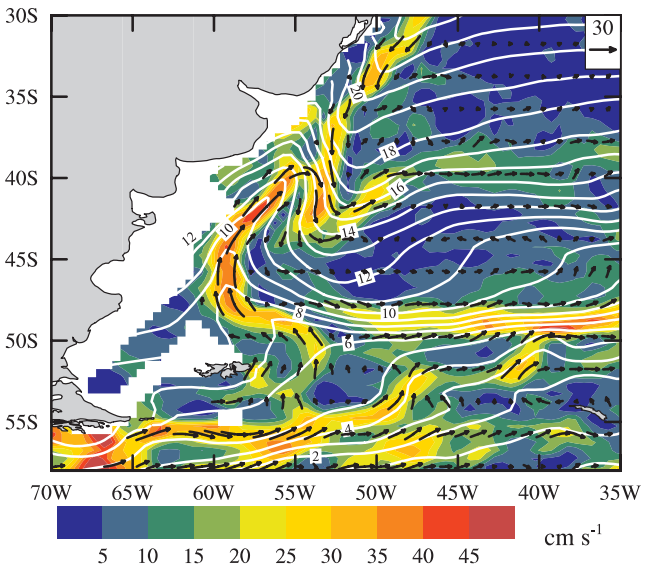

Fig. 1. Mean geostrophic ocean current velocity (arrows in cm s^{-1}) and speed (color in cm s^{-1}) based on drifter and satellite altimeter observations. Annual mean climatology of AVHRR SST is superimposed in contours at 1°C intervals.

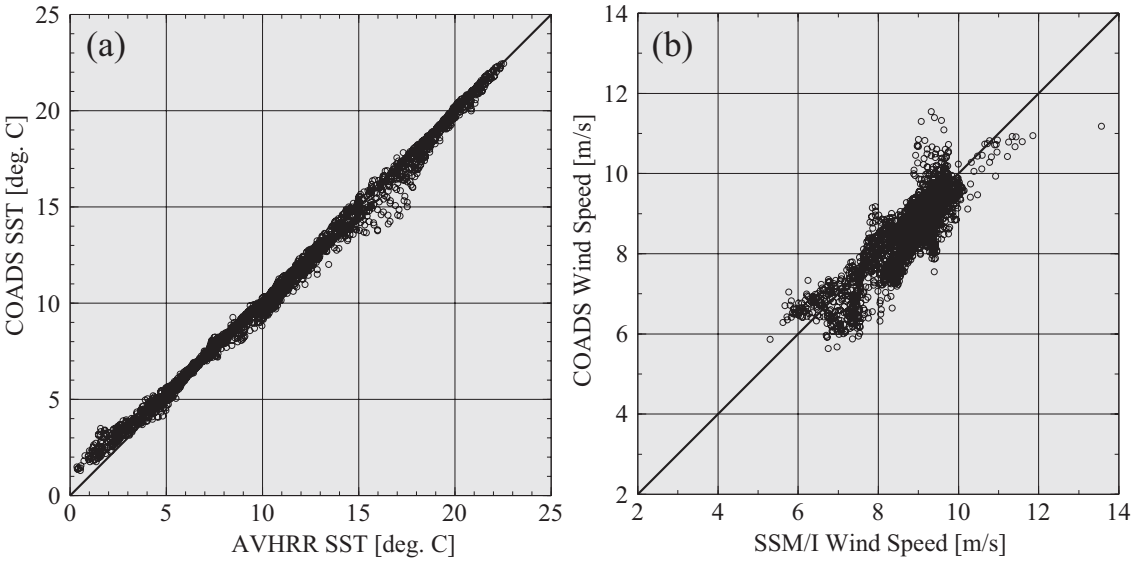

Fig. 2. Scatter plots for comparison of annual mean climatologies of SST and surface wind speed over the southwestern Atlantic (40°W – 70°W, 30°S – 58°S): (a) AVHRR and HiRAC SST, and (b) SSM/I and HiRAC wind speed.

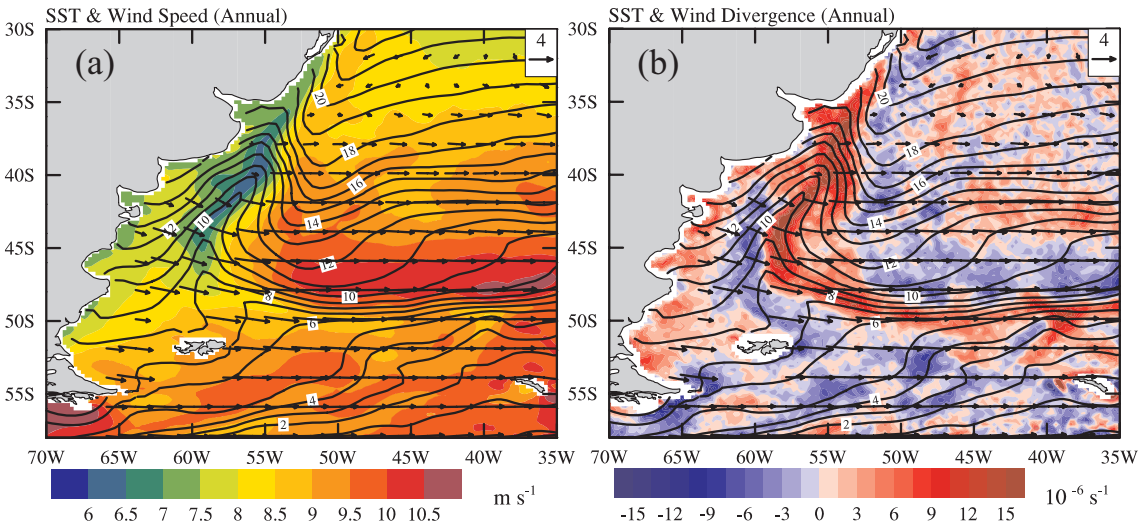

Fig. 3. Annual mean climatologies of (a) scalar wind speed (color in m s^{-1}) and (b) surface wind divergence (color in 10^{-6} s^{-1}) observed by QuikSCAT, superimposed on mean SST (contours in ºC) and surface wind velocity (arrows in m s^{-1}).

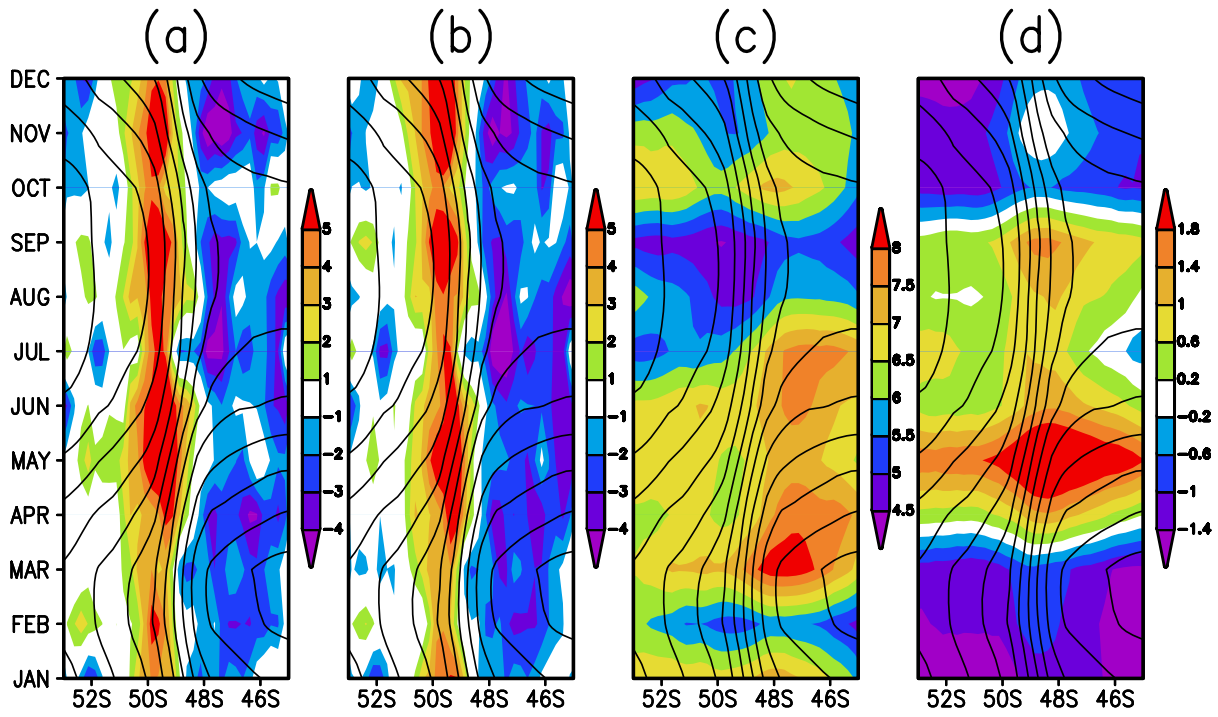

Fig. 4. Climatological annual cycle averaged in 40°W – 50°W. (a) Total surface-wind divergence (10^{-6} s^{-1}), (b) divergence due to the meridional velocity only (10^{-6} s^{-1}), (c) surface zonal and (d) meridional velocities (m s^{-1}). SST contours are superimposed at 1°C intervals.

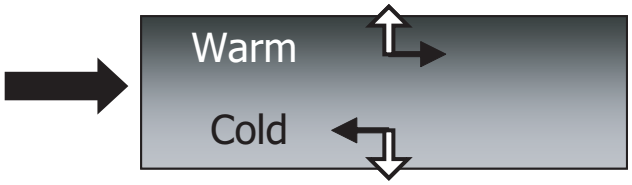

Fig. 5. Schematic for surface wind divergence generated by winds blowing in parallel to the SST front (shaded box). Block arrow on the left: background westerly wind; solid arrows: wind perturbations induced by the SST front; open arrows: meridional winds induced by the Coriolis force acting on the zonal wind perturbations.

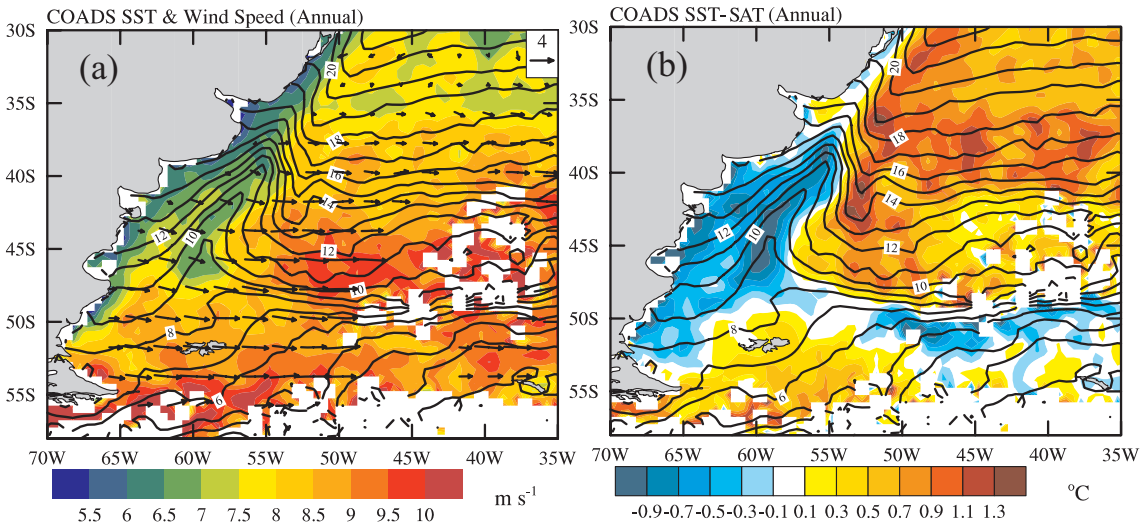

Fig. 6. (a) Same as Fig. 3a but for HiRAC. (b) Sea-air temperature difference (SST-SAT; color in ºC) calculated from HiRAC, superimposed on mean HiRAC SST.

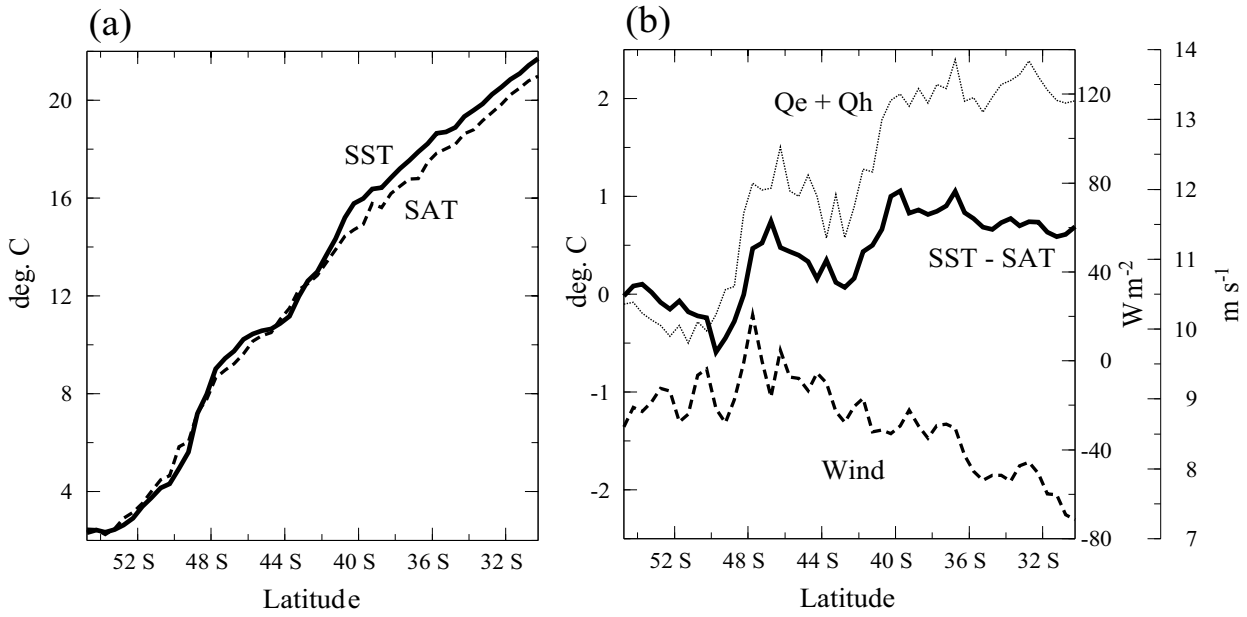

Fig. 7. Cross-frontal structure. (a) SST (solid in ºC) and surface air temperature (dashed in ºC) averaged in 35ºW – 47ºW as a function of latitude. (b) SST-SAT (thick solid in ºC), scalar wind speed (dashed in m s^{-1}), and surface latent and sensible heat fluxes (thin solid in W m^{-2}). All from HiRAC annual-mean climatology.

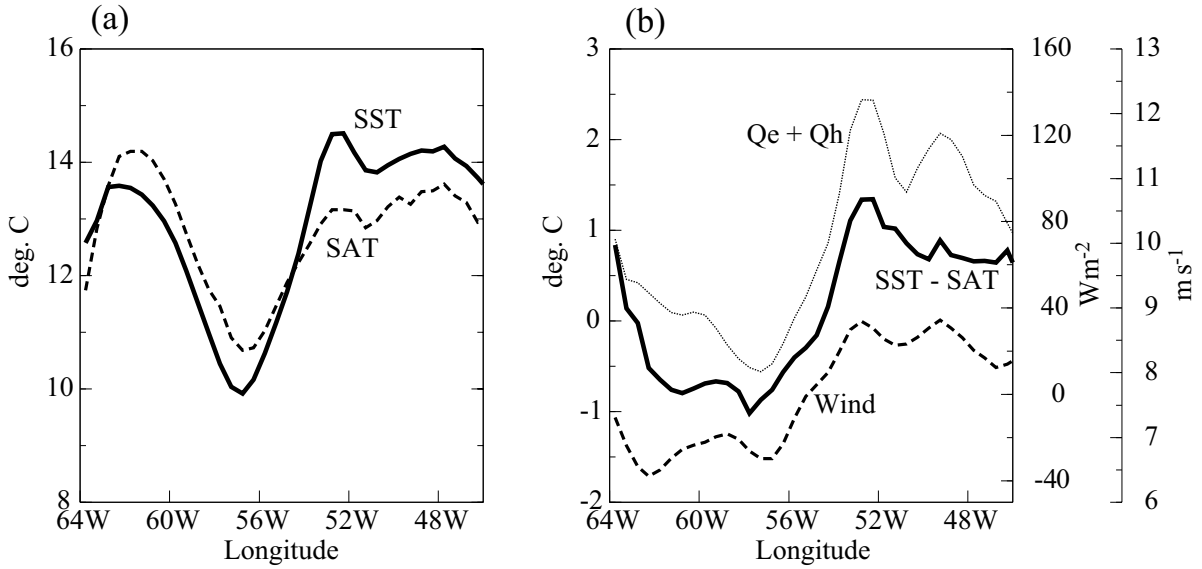

Fig. 8. Same as Fig. 7 but for HiRAC annual-mean climatologies along 42ºS as a function of longitude.

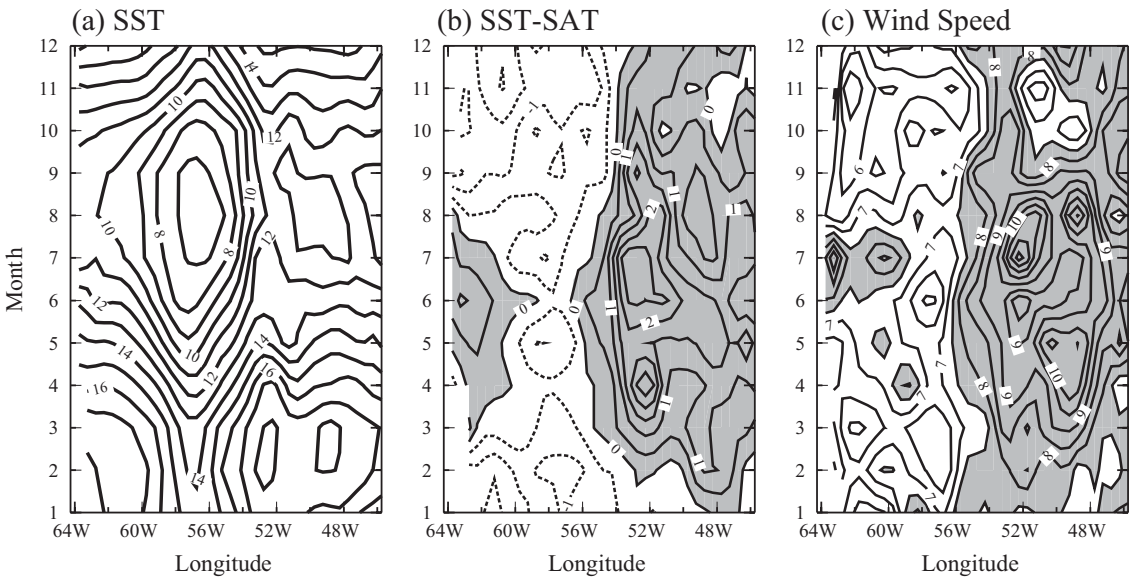

Fig. 9. Annual cycle along 42ºS of (a) SST (contour intervals of 1 ºC), (b) SST-SAT (contour intervals of 0.5 ºC; shading > 0 ºC), and (c) surface wind speed (contour intervals of 0.5 m s^{-1}; shade > 6.5 m s^{-1}) as a function of longitude and calendar month. All from HiRAC climatology.

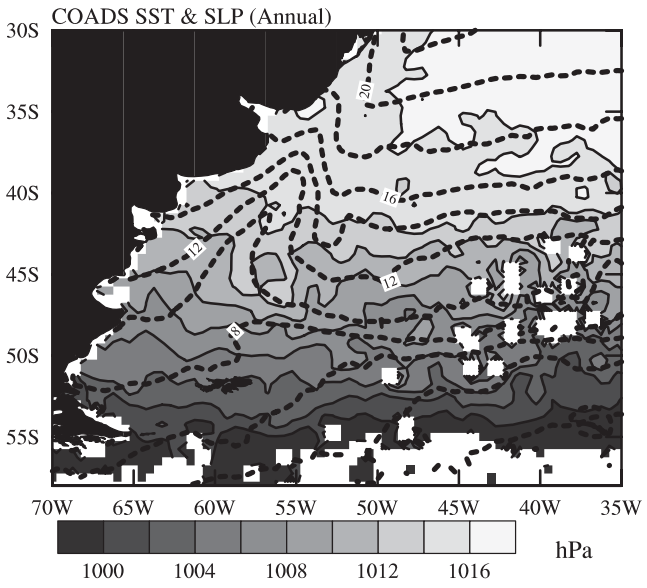

Fig. 10. Same as Fig. 6a but for HiRAC sea level pressure (solid contours and gray shade in hPa), superimposed on mean HiRAC SST (dashed contours at 2ºC intervals).

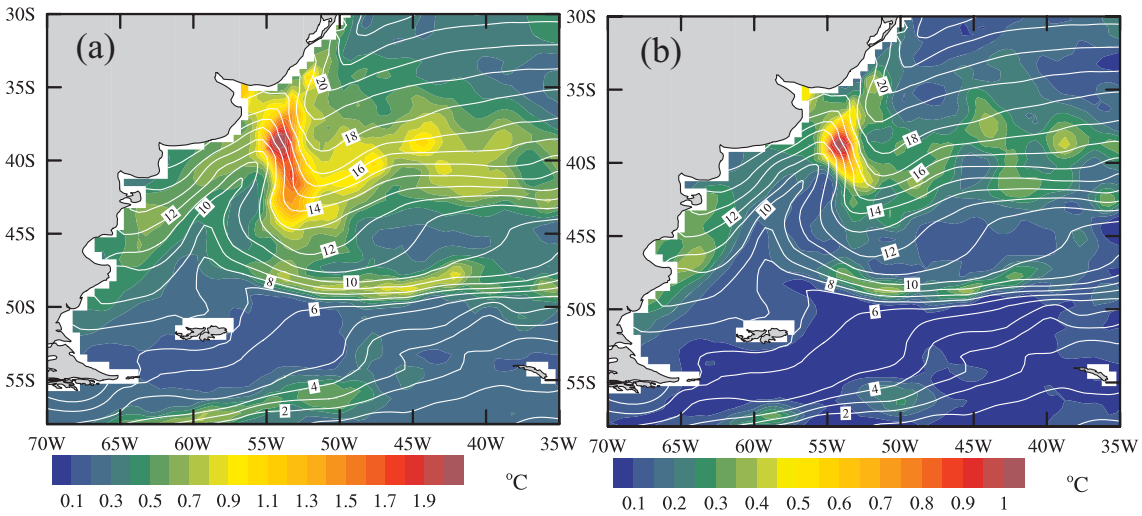

Fig. 11. Standard deviations (color in ºC) for (a) unfiltered and (b) filtered monthly AVHRR SST anomalies, superimposed on mean AVHRR SST white contours at 1 ºC intervals.

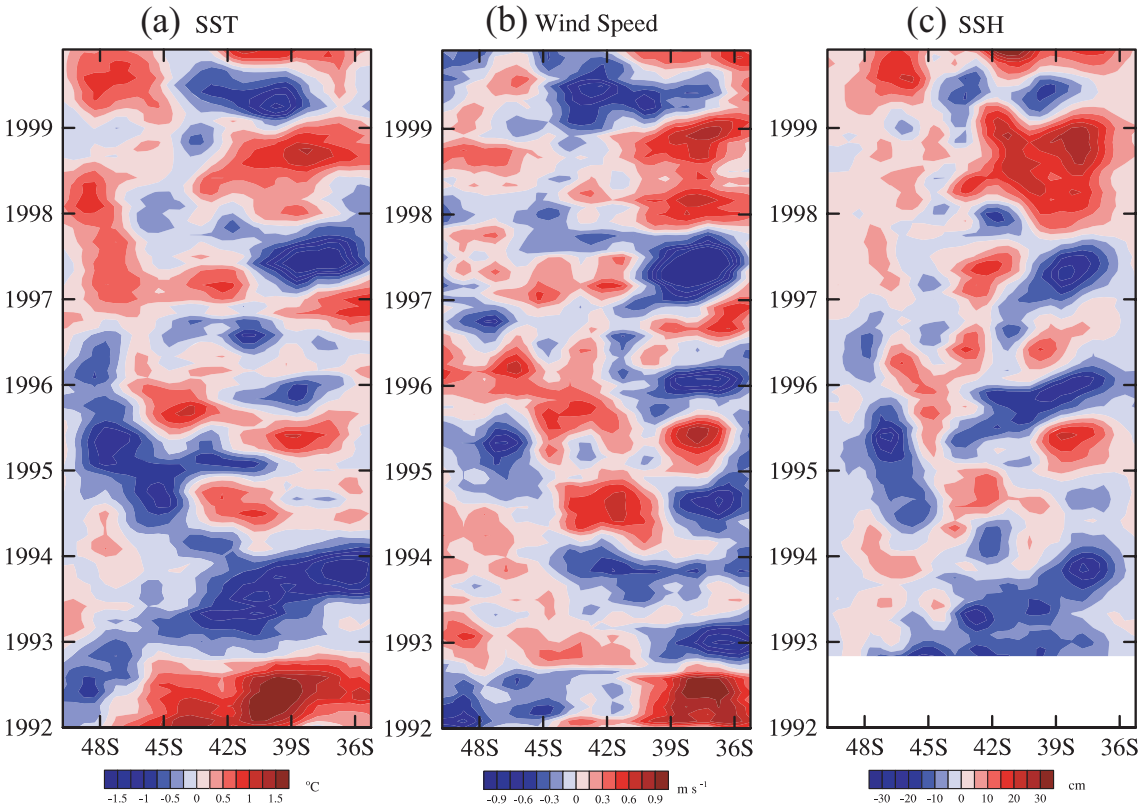

Fig. 12. Latitude-time sections of filtered anomalies of (a) AVHRR SST (ºC), (b) SSM/I scalar wind speed (m s^{-1}), and (c) satellite altimeter SSH (cm) along the meridional SST front at 53.25ºW.

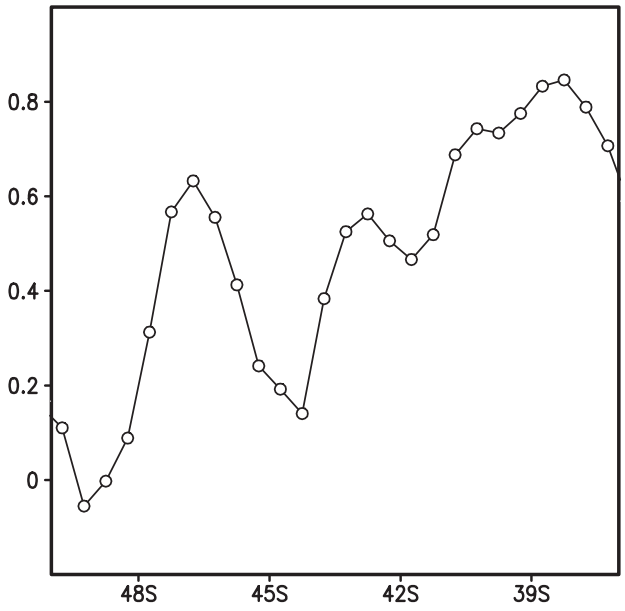

Fig. 13. Correlation coefficient between AVHRR SST and SSM/I surface wind anomalies along 53.25°W.

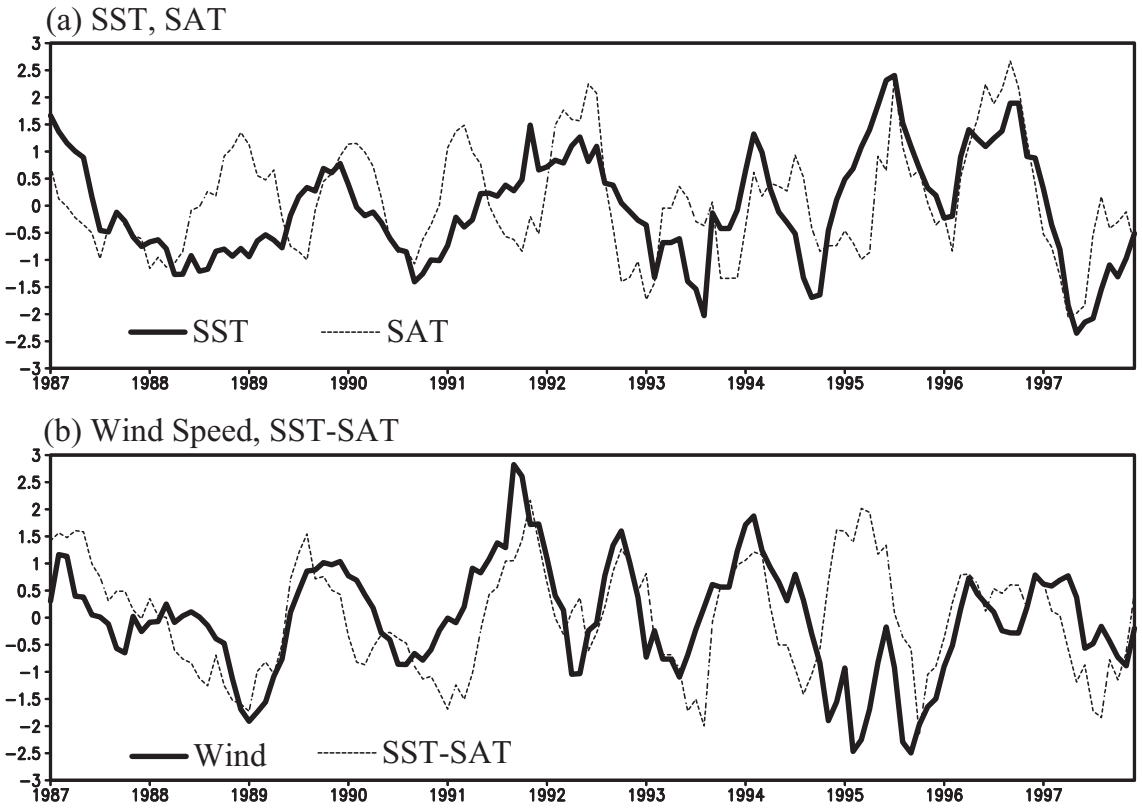

Fig. 14. Time series of anomalies of (a) SST (solid) and SAT (dashed), and (b) SST-SAT (solid) and scalar wind speed, averaged in a region of maximum SST variance (53.25°W, 36°S – 39°S). All from HiRAC and normalized with their respective standard deviations.

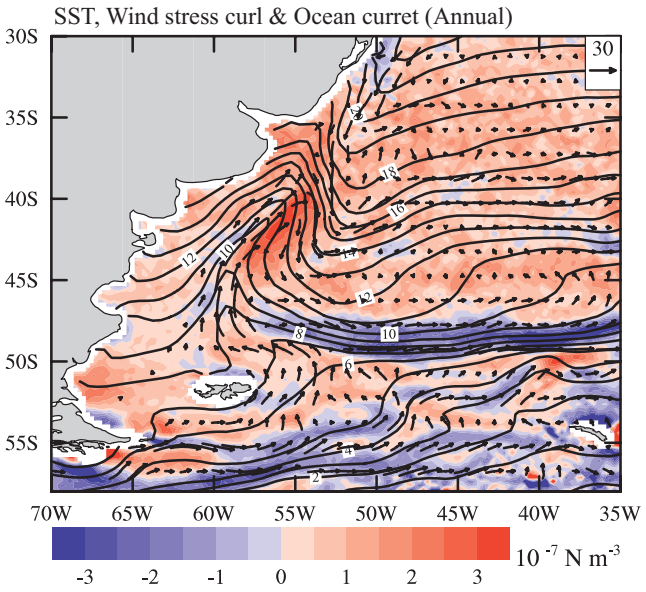
SST, Wind stress curl & Ocean curret (Annual)
30S
35S
40S
45S
50S
55S
70W
65W
60W
55W
50W
45W
40W
35W
30
-3
-2
-1
0
1
2
3
10 -7 N m-3